INTERPRETATION OF DIFFUSIVE AND NONDIFFUSIVE TRANSPORT IN TOKAMAK EDGE PEDESTAL MEASUREMENTS

W. M. STACEY*

Georgia Institute of Technology, Fusion Research Center, Atlanta, Georgia 30332-0745

Received June 27, 2012
Accepted for Publication August 14, 2012

A formalism, based on particle, momentum, and energy balance constraints, for the interpretation of diffusive and nondiffusive transport from plasma edge measurements is presented and applied to interpret transport differences between low-mode and high-mode DIII-D [J. Luxon, Nucl. Fusion, Vol. 42, p. 614 (2002)] plasmas. The experimental values of basic transport properties (thermal diffusivities and momentum transport frequencies) inferred for H-mode and L-mode are compared with each other and with "classical" predictions. Once the basic transport mechanisms are ascertained by such comparison of theoretical predictions with experimental inference, the presented formalism will provide a first-principles predictive model for density, temperature, velocity, and pressure profiles in the edge pedestal.

KEYWORDS: *edge transport, diffusive/nondiffusive transport, edge pedestal*

Note: Some figures in this paper are in color only in the electronic version.

I. INTRODUCTION

Although it has long been recognized that the characteristics of the edge plasma are important for achieving good global tokamak performance[1,2] and tokamak edge pedestal physics has long been an active area of tokamak physics research (e.g., as summarized in Ref. 3), the physics of the tokamak edge pedestal remains an active area of plasma physics research (e.g., as summarized in Ref. 4). The physics of the edge pedestal may be categorized as (a) the physics of the transport processes that determine the density, temperature, and velocity profiles in the absence of or between edge-localized modes (ELMs) and (b) the physics of the magnetohydrodynamic (MHD) instabilities that set a limiting pressure gradient for the onset of ELMs.

While there is a growing consensus that the limiting values of pedestal pressure gradients are determined by an interaction of MHD peeling-ballooning mode and kinetic ballooning mode instabilities,[5] the transport processes causing the pedestal structure (pressure, density, and temperature profiles) in the absence of ELMs or between ELMs remain an open question. These transport processes arise from three different types of phenomena: (a) collisional or fluctuation phenomena that drive particle, momentum, and energy fluxes; (b) force (momentum) and energy-flux balance requirements that determine pressure and temperature gradients; and (c) the loss of charged particles from the plasma by other mechanisms.

A relationship between changes in the radial electric field E_r and in the poloidal rotation velocity V_θ in the plasma edge, on one hand, and changes in the pressure, temperature, and density gradients in the plasma edge, on the other hand, was one of the earliest experimental H-mode observations,[6] suggesting that the rotation velocities and the radial electric field were related to the profiles in some way. It has been demonstrated recently that changes in these various experimentally observed quantities are correlated by momentum balance requirements.[7–9]

One widely accepted paradigm postulates that the stabilization of electromagnetic microinstabilities and the corresponding reduction in the diffusive transport coefficients for fluctuation-driven fluxes proportional to density and temperature gradients requires the observed steepening in temperature and density gradients in order for these diffusive heat and particle fluxes to remove the input heat and particles (e.g., Refs. 10, 11, and 12). Other

*E-mail: weston.stacey@nre.gatech.edu

investigations suggest that the physics of the edge plasma may be determined, at least in part, by the "free-streaming" ion orbit loss and the drift loss of thermal ions trapped poloidally in the region near the *X*-point that then drift across the separatrix and into the divertor (e.g., Refs. 13 through 28). Ionization of recycling neutral atoms (e.g., Refs. 29 and 30) and a large variety of small-scale MHD instabilities (e.g., kinetic ballooning mode discussed in Ref. 31) also have been suggested as causes of the observed structure in the density and temperature profiles in the edge pedestal of tokamak plasmas.

In order to interpret experimental results, we take a somewhat different, more holistic, approach. We postulate that (a) particle densities must satisfy particle balance equations taking into account particle sources and sinks, (b) particle fluxes must satisfy force (momentum) balance equations, (c) energy fluxes must satisfy "energy-force" (or "energy-flux") balance equations, and (d) energy densities must satisfy energy balance equations that take into account energy sources and sinks. We interpret the experimental data on particle and temperature profiles in terms of the requirements imposed by these physical constraints.

In particular, radial and toroidal momentum balance requires that the pressure gradient be balanced by the E_{rad}, $V \times B$ and smaller radial forces $L_{pi}^{-1} \equiv -dp_i/p_i\,dr = (V_{ri} - V_{pri}(E_r, V_\theta, \ldots))/D_i(\nu_{ik}, \nu_{cx}, \nu_{visc}, \ldots)$, and the heat conduction relation (a surrogate for the energy-flux balance equation) requires $L_{Ti,e}^{-1} = q_{i,e}/n_{i,e}T_{i,e}\chi_{i,e}$. The ion density gradient then follows from $L_{ni}^{-1} = L_{pi}^{-1} - L_{Ti}^{-1}$. Here, $D_i \equiv (m_i T_i \nu_{ik}/(e_i B_\theta)^2)(1 + (\nu_{cxi} + \nu_{visci} + \nu_{anomi})/\nu_{ik} - e_i/e_k)$ is the "diffusion coefficient," and $V_{pri} = [-M_{\phi i} - n_i e_i E_\phi^A + n_i m_i(\nu_{ik} + \nu_{cxi} + \nu_{visci} + \nu_{anomi})(B_\phi V_{\theta i} + E_{rad})/B_\theta - n_i m_i \nu_{ik} V_{\phi k}]/n_i e_i B_\theta$ is the "pinch velocity."

This formalism provides a means for interpreting the "transport coefficients"—heat diffusivities $\chi_{i,e}$ and angular momentum transport frequencies due to interspecies collisions ν_{jk}, viscosity ν_{visc}, charge exchange ν_{cx}, and "anomalous" fluctuation processes ν_{anom}—from measured temperatures, densities, and rotation velocities. These inferred experimental transport coefficients can be compared against various theoretical models for the respective transport processes. Once the transport coefficients are ascertained, this formalism will provide a first-principles predictive model for the edge pedestal pressure, density, temperature, and velocity profiles.

In this paper, we describe the formalism and apply it to interpret diffusive and nondiffusive transport processes in DIII-D (Ref. 32).

II. MULTIFLUID PARTICLE, MOMENTUM, AND ENERGY TRANSPORT EQUATIONS

In this section, a multifluid plasma transport theory that determines the density, temperature, and velocity profiles in the edge plasma and that conserves particles, momentum, and energy is formulated systematically from the first four velocity moments of the Boltzmann transport equation. The important transport coefficients needed in order to solve these equations are identified, but these transport coefficients must be determined from experiment or a higher-order theory. In order to keep the formalism as simple as possible, we assume one-dimensional radial transport in a slab approximation.

The first velocity moment of the distribution function is the particle density, and the first velocity moment equation of the Boltzmann equation is the continuity, or particle balance, equation for the species *j*:

$$\frac{\partial(n_j V_{rj})}{\partial r} = -\frac{\partial n_j}{\partial t} + n_e n_o \langle \sigma v \rangle_{ion} + S_{nb} \ , \qquad (1)$$

where

$n_e n_o \langle \sigma v \rangle_{ion}$ = ionization source of recycling neutrals

S_{nb} = neutral beam source of species *j*.

Similar equations obtain for other ion species *k* present in the plasma, and the electron density n_e is constrained by quasi-neutrality. Typical of moments equations, this first moment equation contains not only the first velocity moment of the distribution function—the density n_j—but also the second velocity moment—the average radial velocity V_{rj}, in the form of the average radial particle flux $\Gamma_j = n_j V_{rj}$.

The toroidal and radial components of the second velocity moment, or momentum balance, equation may be written, respectively, for any ion species *j*:

$$n_j m_j[(\nu_{jk} + \nu_{dj})V_{\phi j} - \nu_{jk} V_{\phi k}] = n_j e_j E_\phi^A + n_j e_j B_\theta V_{rj} + M_{\phi j} \qquad (2)$$

and

$$V_{\phi j} = \frac{1}{B_\theta}\left[E_r + V_{\theta j} B_\theta - \frac{1}{n_j e_j}\frac{\partial p_j}{\partial r}\right] , \qquad (3)$$

where

k = sum over other ion species, in general

E_ϕ^A = electromagnetically induced toroidal electric field

$M_{\phi j}$ = toroidal momentum input to species *j*

ν_{dj} = toroidal angular momentum transfer frequency, which represents the combined effect of viscosity, inertia, atomic physics, and other anomalous processes, but not friction, which is treated separately.

Justification for representing the toroidal momentum transfer processes in this form is discussed in Ref. 33. Equations (2) and (3) contain the third velocity moment of the

distribution function, the pressure (or equivalently the temperature).

The third velocity moment, or energy balance, equations for the ion species and electrons, Eqs. (4) and (5), respectively, determine the ion and electron total energy fluxes $Q_{j,e}$:

$$\frac{\partial Q_j}{\partial r} \equiv \frac{\partial}{\partial r}\left(q_j + \frac{3}{2}\Gamma_j T_j\right) = -\frac{\partial}{\partial t}\left(\frac{3}{2} n_j T_j\right) + q_{nbj} - R_{je} - n_e n_o^c \langle \sigma v \rangle_{cx} \frac{3}{2}(T_j - T_o^c) \tag{4}$$

and

$$\frac{\partial Q_e}{\partial r} \equiv \frac{\partial}{\partial r}\left(q_e + \frac{3}{2}\Gamma_e T_e\right) = -\frac{\partial}{\partial t}\left(\frac{3}{2} n_e T_e\right) + q_{nbe} + R_{je} - n_e n_k L_k(T_e) \ , \tag{5}$$

where

q_{nb} = neutral beam (or other) heating

R_{je} = ion-to-electron collisional energy transfer

$n_e n_o^c \langle \sigma v \rangle_{cx}$ = charge-exchange cooling of the ions

$n_e n_k L_k$ = radiation cooling of the electrons.

Equations (4) and (5) contain the fourth velocity moment of the distribution function, the conductive heat fluxes $q_{j,e}$.

In principle, the fourth moment equations (the energy-flux or energy-force equations) could be solved for the conductive heat fluxes $q_{j,e}$, but these equations are rather formidable,[34] involving complex tensor differential relations among the lower velocity moments, and the next higher, fifth-order velocity moment of the distribution function is involved. In practice, these fourth-order velocity moment equations are replaced by the surrogate closure relations for conductive heat fluxes:

$$q_{j,e} = -n_{j,e}\chi_{j,e}\frac{\partial T_{j,e}}{\partial r} \ , \tag{6}$$

which can be used to determine the temperature profiles, thus closing the set of four moments equations.

The "basic transport coefficients" appearing in Eqs. (1) through (5) are the interspecies collisional momentum transfer frequencies ν_{jk}, the toroidal angular momentum transport frequencies $\nu_{dj} = \nu_{viscj} + \nu_{cxj} + \nu_{inertj} + \nu_{anomj}$ (with viscous, charge-exchange, inertial, and anomalous components), and the thermal diffusivities $\chi_{j,e}$. These basic transport coefficients must be determined from higher-order calculations or experiment.

III. CONSTRAINTS ON DENSITY, TEMPERATURE, AND PRESSURE PROFILES IN EDGE PLASMAS

Equations (1) through (5) provide first-principles constraints on the density, temperature, and pressure profiles in the edge plasma, between or in the absence of ELMs. The consequences of these constraints are developed in this section for the situation in which there is a main ion species j and a single impurity species k with the same logarithmic density derivative and the same local temperature as the main ions, in which case Eqs. (2) and (3) can be combined to arrive at a constraint on the main ion pressure gradient:

$$L_{pj}^{-1} \equiv -\frac{1}{p_j}\frac{\partial p_j}{\partial r} = \frac{V_{rj} - V_{rj}^{pinch}}{D_j} \ , \tag{7}$$

where the diffusion coefficient is

$$D_j \equiv \frac{m_j T_j \nu_{jk}}{(e_j B_\theta)^2}\left(1 + \frac{\nu_{dj}}{\nu_{jk}} - \frac{e_j}{e_k}\right) \tag{8}$$

and the pinch velocity

$$V_{rj}^{pinch} \equiv \frac{\left[-M_{\phi j} - n_j e_j E_\phi^A + n_j m_j(\nu_{jk} + \nu_{dj}) \times (f_p^{-1} V_{\theta j} + E_r/B_\theta) - n_j m_j \nu_{jk} V_{\phi k}\right]}{n_j e_j B_\theta} \tag{9}$$

is a collection of normalized forces associated with the electric field, $V \times B$ forces, and beam momentum input. The fundamental transport coefficients that determine the main ion diffusion coefficient are the momentum exchange frequencies with impurities ν_{jk} and with neutrals ν_{cx}, and the momentum transport frequencies across flux surfaces due to viscosity and inertia, and to any anomalous momentum exchange processes (included in ν_{dj}). Somewhat more complicated expressions result for the general case of multiple impurity species with separate logarithmic density gradients.[33]

The temperature gradients are constrained by Eq. (6):

$$L_{Tj,e}^{-1} \equiv \frac{-1}{T_{j,e}}\frac{\partial T_{j,e}}{\partial r} = \frac{q_{j,e}}{n_{j,e} T_{j,e} \chi_{j,e}} \ , \tag{10}$$

and the density gradients are constrained by $L_n^{-1} = L_p^{-1} - L_T^{-1}$. The profiles are then calculated by integrating these expressions for the gradient scale lengths over the edge pedestal, subject to boundary conditions at the core-pedestal interface or at the separatrix.

IV. PARTICLE AND ENERGY TRANSPORT FLUX CONSTRAINTS IN THE EDGE PEDESTAL

The momentum balance requirement of Eq. (7) can be rearranged into a form that clearly exhibits the diffusive and the nondiffusive components of the radial particle flux:

$$\Gamma_j \equiv n_j V_{rj} = -\frac{n_j D_j}{p_j}\frac{\partial p_j}{\partial r} + n_j V_{rj}^{pinch}$$

$$= -D_j \frac{\partial n_j}{\partial r} - D_j \frac{n_j}{T_j}\frac{\partial T_j}{\partial r} + n_j V_{rj}^{pinch} \quad . \tag{11}$$

In this form, the diffusion coefficient and the pinch velocity appear as "composite transport coefficients," but they both depend upon the basic transport coefficients, i.e., the momentum transport frequencies. The pinch velocity also depends on the electromagnetic and other forces, as required by momentum balance and given by Eqs. (8) and (9). The more general case when the assumption made above about the impurity distribution is not made is treated in Ref. 33.

The conductive heat flux needed to evaluate the temperature gradient in Eq. (10) can be obtained by subtracting the convective heat flux $3/2\Gamma_{j,e}T_{j,e}$, constructed with the solution of Eq. (1), from the total heat flux $Q_{j,e}$ obtained by solving Eqs. (4) and (5):

$$q_{j,e} = Q_{j,e} - \tfrac{3}{2}\Gamma_{j,e}T_{j,e} \quad . \tag{12}$$

The ion particle flux calculated from Eq. (1) includes not only particles being diffusively and convectively transported outward, as indicated in Eq. (11), but also particles that are free-streaming outward on drift orbits that cross the separatrix. If such particles charge-exchange with recycling neutrals, or collide with plasma ions in the scrape-off layer and are swept into the divertor or intersect the chamber wall, they are lost from the plasma. This ion orbit loss can be represented[27] as radially cumulative particle F_{orb} and energy E_{orb} loss fractions, which enables the ion conductive heat flux to be written in a form that takes into account ion orbit loss:

$$q_j = Q_j(1 - E_{orbj}) - \tfrac{3}{2}\Gamma_j(1 - F_{orbj})T_j \quad , \tag{13}$$

where Γ_j and Q_j are the ion particle and heat fluxes obtained by solving Eqs. (1) and (4), respectively.

We note that the presence of ion orbit loss implies the existence of a compensating nonambipolar mechanism to maintain charge neutrality, which we have not explicitly included because we do not know what it is. However, a plausible effect of such a mechanism is to create a radial current in the plasma that alters the radial electric field. Since we use a radial electric field inferred from experimental data, it is plausible that the effect of this compensating mechanism is thereby implicitly taken into account.

V. INTERPRETATION OF EXPERIMENTAL TRANSPORT COEFFICIENTS

In an interpretive analysis, the experimental values of the thermal diffusivities can be inferred[35] from the measured density and temperature profiles:

$$\chi_{j,e}^{\exp} = -\frac{q_{j,e}^{\exp}}{n_{j,e}^{\exp}(\partial T_{j,e}^{\exp}/\partial r)} = -\frac{(Q_{j,e}^{\exp} - 1.5\Gamma_{j,e}^{\exp}T_{j,e}^{\exp})}{n_{j,e}^{\exp}(\partial T_{j,e}^{\exp}/\partial r)} \quad , \tag{14}$$

when $Q_{j,e}^{\exp}$ is obtained by solving Eq. (4) or (5) for the total heat flux, $\Gamma_j^{\exp}$ is obtained by solving Eq. (1) for the total radial particle flux, and from there $\Gamma_e^{\exp}$ is constructed taking into account impurities. In the case of ions, the ion orbit loss should be taken into account by using Eq. (13) for the numerator in Eq. (14).

In principle, the composite momentum transport frequency ν_{dj} for each ion species can be inferred from the toroidal momentum balance Eq. (2) for that species, if the toroidal rotation velocities for all species are measured, but this is not presently the case for the main ion species: deuterium. When such measurements of main ion rotation velocities become common, this will be the preferred method for their determination from experiment.

At present, the electron density and temperature profiles are measured (by Thomson scattering, e.g., Ref. 36), and the carbon density, temperature, and rotation velocities are measured [by charge-exchange recombination (CER), e.g., Ref. 37]. From the measurement of the carbon pressure profile gradient and of the carbon toroidal and poloidal rotation velocities, the radial electric field can be determined from the radial force balance Eq. (3) for carbon. The toroidal electric field E_ϕ^A can be determined from measurement, and the toroidal neutral beam momentum input $M_{\phi j}$ can be calculated. For a deuterium plasma with a dominant carbon impurity, this leaves the deuterium toroidal velocity as the only unknown quantity that prevents the two toroidal Eqs. (4) for deuterium and carbon being solved simultaneously to determine ν_{dj} and ν_{dk}.

In order to deal with this situation, we employ the standard perturbation theory approach that is widely used in plasma physics (e.g., the various ordering arguments). If the collisional friction coupling term is large relative to the viscous term, the carbon and deuterium toroidal rotation velocities should be similar, which suggests a perturbation analysis with this velocity difference as the small parameter. Using such a perturbation analysis[38] leads to estimates of the experimental values of the toroidal angular momentum transfer frequencies ν_{dj} for the deuterium ions,

$$\nu_{dj} = \frac{\begin{pmatrix}(n_j e_j E_\phi^A + e_j B_\theta \Gamma_j + M_{\phi j}) \\ + (n_k e_k E_\phi^A + e_k B_\theta \Gamma_k + M_{\phi k})\end{pmatrix}}{(n_j m_j + n_k m_k)V_{\phi k}^{\exp}} \quad , \tag{15}$$

and ν_{dk} for the carbon impurity ions,

$$\nu_{dk} = \frac{\begin{pmatrix}(n_k e_k E_\phi^A + e_k B_\theta \Gamma_k + M_{\phi k}) \\ + n_j m_j \nu_{jk} (V_{\phi j} - V_{\phi k})_0\end{pmatrix}}{n_k m_k V_{\phi k}^{\exp}} \quad , \tag{16}$$

where

$$(V_{\phi j} - V_{\phi k})_0 = \frac{\begin{pmatrix}(n_j e_j E_\phi^A + e_j B_\theta \Gamma_j + M_{\phi j}) \\ - n_j m_j \nu_{dj} V_{\phi k}^{\exp}\end{pmatrix}}{n_j m_j (\nu_{jk} + \nu_{dj})} \tag{17}$$

is the first-order perturbation estimate of the difference in deuterium and carbon toroidal rotation velocities. The perturbation estimate of the difference between the main ion and (measured) carbon rotation velocities provides an indication of the validity or invalidity of the perturbation theory for a particular application—we have calculated some DIII-D shots in which the difference in the velocities was comparable to the measured carbon velocity, for which the perturbation theory should not be trusted, and other cases (including the one in this paper) where the perturbation calculation of the difference in velocities was small, indicating that the result could be trusted.

We momentarily digress to comment on recent progress on the measurement of deuterium rotation from D_α spectra and with probes, vis-à-vis the perturbation analysis. Grierson et al.,[39] in their first D_α measurements on DIII-D, found similar toroidal rotation velocity profiles for carbon and deuterium in a standard H-mode discharge; most recently,[40] they reported similar toroidal rotation profiles for carbon and deuterium ions measured in a standard L-mode shot, but they found some differences in carbon and deuterium profiles for intrinsic rotation in an electron cyclotron heated plasma and in a plasma with an internal transport barrier. The probe measurements of Boedo et al.[41] and Mueller et al.[42] found a thin layer of co-rotation in the deuterium rotation profile just inside the separatrix that is not discernible in the carbon CER data, which may be due to ion orbit loss of deuterium, as suggested by the authors. The sort of small differences between deuterium and carbon toroidal rotation reported by Grierson et al.[39,40] are of the same magnitude that we usually find from perturbation analyses of DIII shots, including the one in the present paper.

All of the experimental parameters needed to infer the experimental values of the basic transport coefficients are now available. With these parameters, the composite diffusion coefficient of Eq. (8) can be evaluated. The only remaining parameter needed in order to infer the experimental pinch velocity of Eq. (9) is the deuterium poloidal velocity. Our experience with calculating poloidal rotation velocities, using neoclassical parallel viscosity models,[43] was that the deuterium and carbon velocities differ too much to use a perturbation analysis and that the calculated carbon velocity did not agree too well with the measured values in the steep gradient region of the edge plasma, perhaps indicating a missing torque term in the standard poloidal momentum balance equation. Thus, we use instead the radial momentum balance Eq. (3) for the deuterium ions, with the radial electric field determined from the same equation for carbon ions, and with the toroidal rotation velocity for deuterium determined by adding Eq. (17) to the toroidal rotation velocity measured for carbon ($j = D$; $k = C$), to obtain

$$\begin{aligned} V_{\phi j}^{\exp} &= V_{\phi k}^{\exp} + (V_{\phi j} - V_{\phi k})_0 \\ &= V_{\phi k}^{\exp} + \frac{(n_j e_j E_\phi^A + e_j B_\theta \Gamma_j + M_{\phi j}) - n_j m_j \nu_{dj} V_{\phi k}^{\exp}}{n_j m_j (\nu_{jk} + \nu_{dj})} \quad . \end{aligned} \tag{18}$$

This expression can be used in the radial momentum balance equation to evaluate the experimental deuterium poloidal rotation velocity

$$V_{\theta j}^{\exp} = -\frac{E_r^{\exp}}{B_\theta} + \frac{B_\theta}{B_\phi} V_{\phi j}^{\exp} + \frac{1}{n_j e B_\theta} \frac{\partial p_j}{\partial r} \quad . \tag{19}$$

The deuterium pressure gradient can be determined experimentally from the measured carbon and electron pressure gradients.

We are now able to determine all of the basic and composite transport parameters from experiment, for comparison with various theoretical models.

VI. COMPARISON OF DIII-D L-MODE AND H-MODE TRANSPORT COEFFICIENTS

As an application of the above formalism, we apply it to a comparison of the transport coefficients inferred immediately before and slightly after an L-H transition in DIII-D shot 118897. Fits to the measured densities and temperatures before and after the L-H transition are shown in Fig. 1.

Ion orbit loss cumulative loss fractions calculated using the methodology of Ref. 27 are shown in Fig. 2. The cumulative loss fractions increase rapidly with radius just inside the separatrix and are rather similar in L-mode and H-mode.

The experimental electron and ion thermal diffusivities, inferred as discussed in connection with Eq. (14), are shown in Figs. 3 and 4. For comparison, the corresponding "classical" thermal diffusivities—paleoclassical for electrons and Chang-Hinton neoclassical for ions—are also shown (the formulas given in Ref. 35 for neoclassical and Ref. 40 for paleoclassical were evaluated using the experimental data).

The sharp drop in the inferred experimental ion thermal diffusivities just inside of the separatrix (at $\rho = 1.0$) is due to the ion orbit loss correction of the total energy and particle fluxes. The neoclassical ion thermal

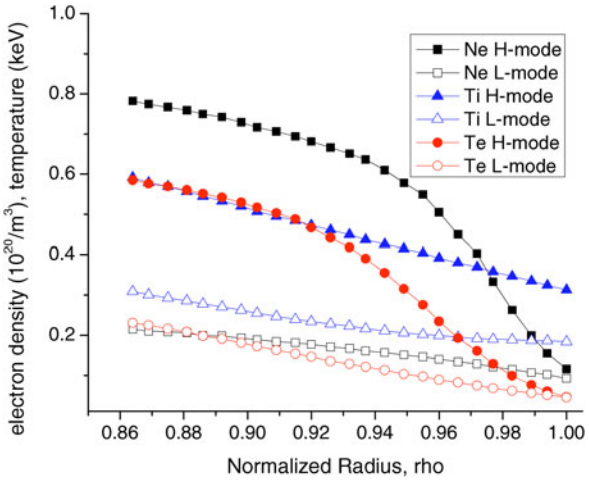

Fig. 1. Fits of measured electron density, and ion and electron temperatures in L-mode and H-mode.

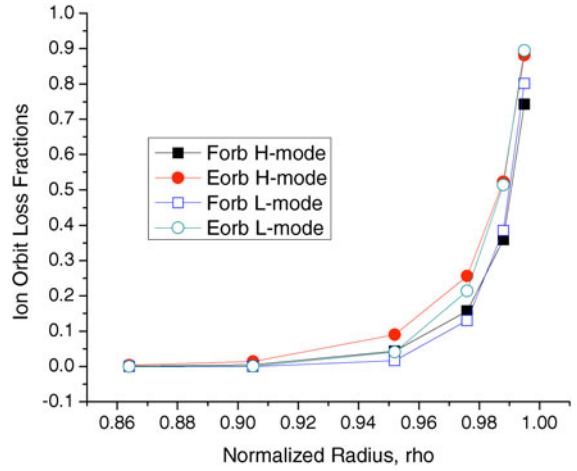

Fig. 2. Calculated cumulative particle and energy loss fractions due to ion orbit loss.

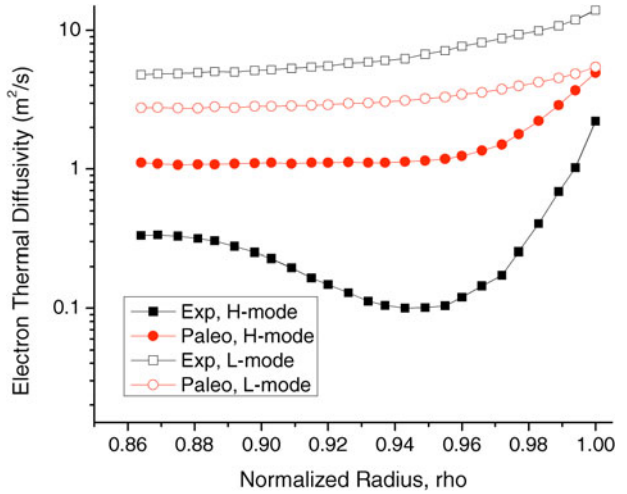

Fig. 3. Electron thermal diffusivities inferred from measured data using Eq. (14) and corresponding paleoclassical predictions using measured data of Fig. 1.

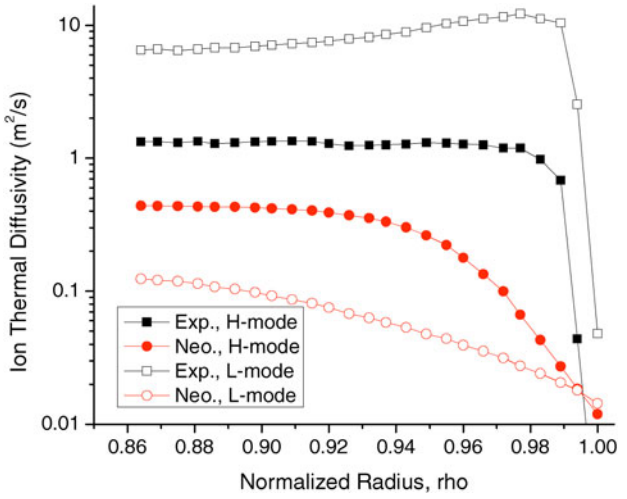

Fig. 4. Ion thermal diffusivities inferred from measured data using Eq. (14) and corresponding neoclassical predictions using experimental data of Fig. 1.

diffusivity, which should set a lower limit on transport, underpredicts the measured value for both L-mode and H-mode, indicating the presence of anomalous fluctuation-driven ion transport mechanisms. The paleoclassical electron thermal diffusivity, which also should set a lower limit on transport, underpredicts the measured thermal diffusivity in L-mode, indicating the presence of anomalous transport. However, in H-mode the paleoclassical prediction is greater than the measured electron thermal diffusivity, which would seem to indicate that paleoclassical does not set a lower limit on electron transport.

The measured carbon toroidal rotation velocities and experimental deuterium toroidal rotation velocities, the latter constructed from the perturbation analysis leading to Eq. (18), are plotted in Fig. 5.

The small difference between the measured toroidal rotation velocities for carbon and the constructed experimental toroidal rotation velocities for deuterium supports the use of the perturbation analysis to calculate the latter.

The experimentally inferred toroidal angular momentum transport frequencies ν_{dj}, calculated from Eqs. (15) and (16), are plotted in Fig. 6. The charge-exchange contribution to ν_{dj} was calculated and is also plotted in Fig. 6 to illustrate that it is not large enough to account for the experimental toroidal angular momentum transport rate. It is clear that the experimental ν_{dj} are larger in L-mode

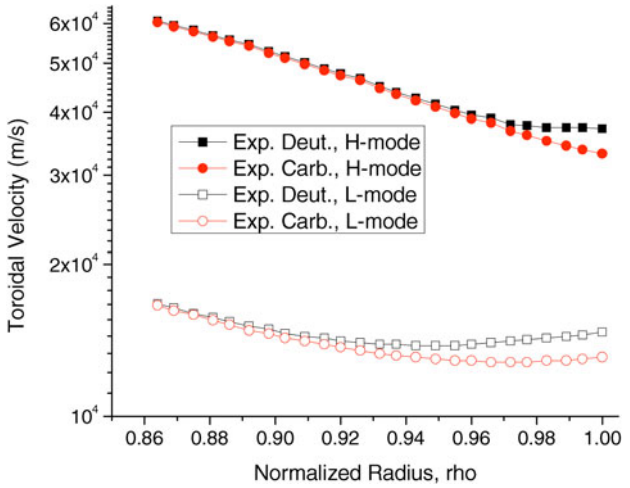

Fig. 5. Experimental toroidal rotation velocities. [Carbon velocities are measured. Deuterium velocities are calculated from Eq. (17) using measured carbon velocities and other data.]

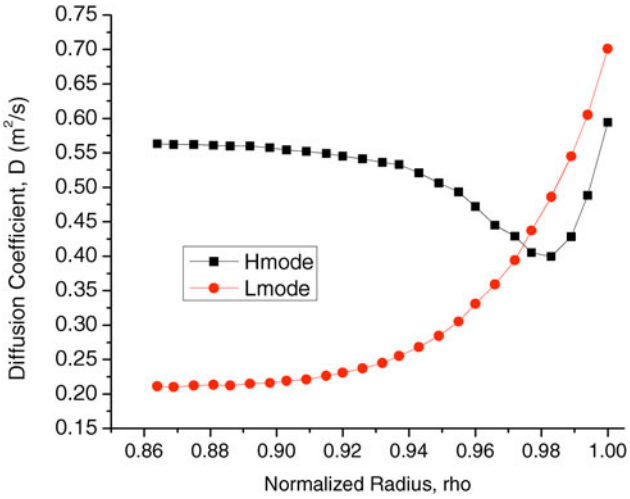

Fig. 7. Deuterium diffusion coefficients evaluated for Eq. (8) using the momentum transport frequencies of Fig. 6.

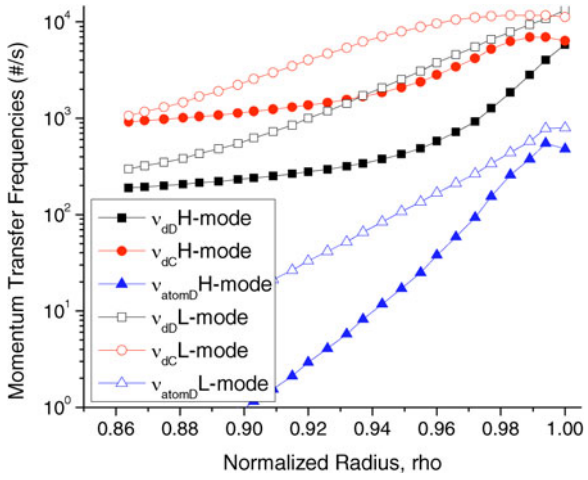

Fig. 6. Toroidal angular momentum transport frequencies calculated from Eqs. (15), (16), and (17) using measured data.

than in H-mode and that they are larger for the carbon impurity ions than for the deuterium ions.

The deuterium diffusion coefficients that result when the ν_{dj} of Fig. 6 and collision frequencies ν_{jk} calculated using the experimental data of Fig. 1 are used to evaluate Eq. (8) are plotted in Fig. 7. It is interesting that the dip in the H-mode diffusion coefficient is reminiscent of results that have been attributed to a transport barrier but that in this case results from the interplay of the increasing (with radius) ν_{dj} and the decreasing ν_{jk}. It is also interesting that the diffusion coefficient is larger in H-mode than in L-mode over most of the edge pedestal.

The experimental radial electric field, evaluated from the carbon radial momentum balance and measurements of the carbon rotation velocities and pressure gradient, is shown in Fig. 8. There is a rather striking difference between L-mode and H-mode values.

The experimental poloidal rotation velocities, measured for carbon and constructed from the radial force balance for deuterium, are plotted in Fig. 9. There are substantial differences between the carbon and deuterium rotation velocities and substantial differences between the L-mode and H-mode profiles for both. The large increase in deuterium poloidal rotation in H-mode is caused [in the evaluation of the poloidal velocity from

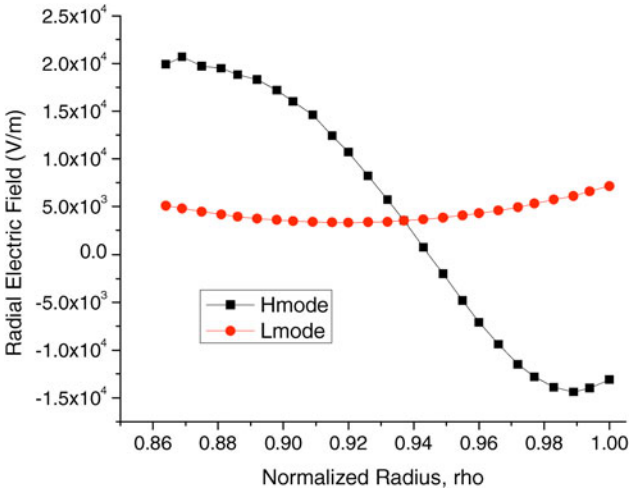

Fig. 8. Radial electric field. (Calculated from radial momentum balance using measured carbon rotation velocities and pressure gradient.)

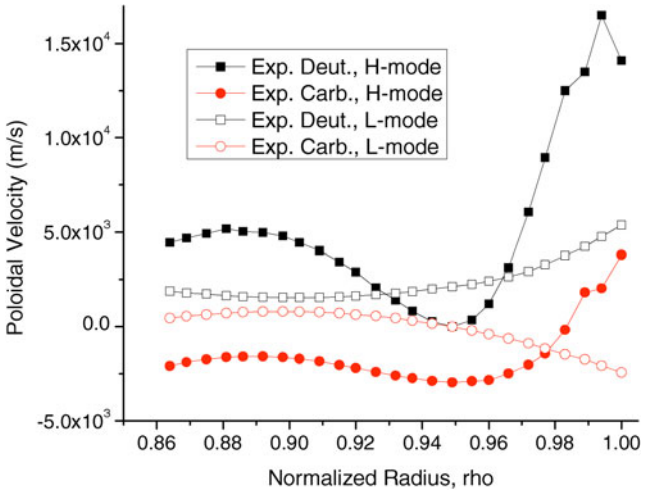

Fig. 9. Poloidal rotation velocities [carbon measured and deuterium evaluated from Eq. (19) using measured data].

the radial momentum balance of Eq. (19), if not physically] by the large negative experimental radial electric field. The cause-and-effect relationship between the poloidal rotation and the radial electric field is an interesting, but unresolved, issue.

The pinch velocities evaluated from Eq. (9) are plotted in Fig. 10. There is a dramatically larger inward pinch just inside the separatrix in H-mode than in L-mode. This pinch is due [in the evaluation of Eq. (9)] to the large values of both the poloidal rotation and of the radial electric field, the effects of which are additive in this case.

Since the main purpose of this paper is to set forth a systematic procedure for interpreting experimental data,

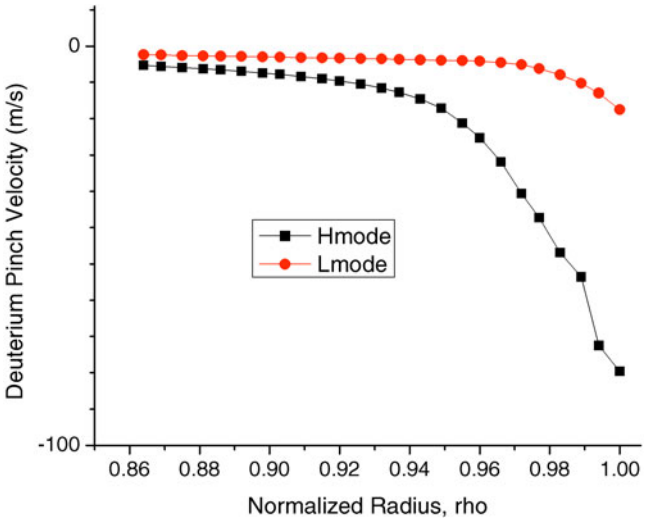

Fig. 10. Pinch velocities evaluated from Eq. (9) using measured data.

we have not done an uncertainty analysis to propagate uncertainties in the various measurements to propagate the uncertainties in measurements through the analysis to calculate uncertainties in quantities like thermal diffusivities and pinch velocities inferred from the experimental data because of the huge amount of time that would be required to do so. However, this uncertainty is definitely an important matter, and much effort goes into minimizing and quantifying experimental errors, as discussed in Ref. 44 and elsewhere. The magnitude of individual experimental errors is also given in Ref. 44 for the types of measurements involved above.

VII. SUMMARY

The first three velocity moments of the Boltzmann equation—continuity, momentum balance, and energy balance—and the heat conduction relation constrain density, temperature, and pressure profiles and determine the form of particle and heat fluxes in the edge pedestal. These constraints require that the particle flux be of a pinch-diffusion form. Momentum exchange, or transport, frequencies and thermal diffusivities are identified as the fundamental transport properties that must be determined from experiment or higher-order calculations.

A formalism was presented for taking these constraints into account in interpreting the fundamental transport properties from experimental measurements, for comparison with theoretical models. An application to the interpretation of the transport properties, both diffusive and nondiffusive, in the L-mode and H-mode phases of a DIII-D shot was discussed, with an emphasis on differences in transport properties associated with the L-mode and H-mode.

Once the fundamental transport properties are resolved in this manner, the formalism will provide a first-principles model for the calculation of density, temperature, and pressure profiles in the edge plasma, between or in the absence of ELMs.

ACKNOWLEDGMENTS

The author is grateful to R. J. Groebner and T. E. Evans for their collaboration in work leading up to this paper and to the former for making available the data used in this analysis. Gratitude is also expressed for the efforts of the DIII-D Team and for the hospitality of General Atomics. This work was supported by the U.S. Department of Energy under grant DE-FG01-ER54538 with the Georgia Tech Research Corporation.

REFERENCES

1. M. KOTSCHENREUTHER et al., *Proc. 16th Conf. Plasma Physics and Controlled Fusion Research*, Montreal, Canada,

October 7–11, 1996, Vol. 2, p. 371, International Atomic Energy Agency (1997).

2. J. E. KINSEY, R. E. WALTZ, and D. P. SCHISSEL, *Proc. 24th Conf. Controlled Fusion and Plasma Physics*, Berchtesgaden, Germany, 1997, Vol. III, p. 1081, European Physical Society (1997).

3. A. E. HUBBARD, *Plasma Phys. Control. Fusion*, **42**, A15 (2000).

4. C. F. MAGGI, *Nucl. Fusion*, **50**, 066001 (2010).

5. P. B. SNYDER et al., *Nucl. Fusion*, **44**, 320 (2004).

6. R. J. GROEBNER, K. H. BURRELL, and R. P. SERAYDARIAN, *Phys. Rev. Lett.*, **64**, 3015 (1990).

7. W. M. STACEY and R. J. GROEBNER, *Phys. Plasmas*, **17**, 112512 (2010).

8. W. M. STACEY and R. J. GROEBNER, *Nucl. Fusion*, **51**, 063024 (2011).

9. W. M. STACEY and T. E. EVANS, *Nucl. Fusion*, **51**, 013007 (2011).

10. H. BIGLARI, P. H. DIAMOND, and P. W. TERRY, *Phys. Fluids B*, **2**, 1 (1989).

11. K. H. BURRELL, *Phys. Plasmas*, **4**, 1499 (1997).

12. P. W. TERRY, *Rev. Mod. Phys.*, **72**, 109 (2000).

13. F. L. HINTON and M. CHU, *Nucl. Fusion*, **25**, 345 (1985).

14. K. MIYAMOTO, *Nucl. Fusion*, **36**, 927 (1996).

15. K. C. SHAING and E. C. CRUME, *Phys. Rev. Lett.*, **63**, 2369 (1989).

16. K. C. SHAING, E. C. CRUME, and W. A. HOULBERG, *Phys. Fluids B*, **2**, 1492 (1990).

17. K. C. SHAING, *Phys. Fluids B*, **4**, 171 (1992).

18. K. C. SHAING, *Phys. Plasmas*, **9**, 1 (2002).

19. G. F. MATTHEWS et al., EFDA-JET-CP(02)01-02, European Fusion Development Agreement (2002).

20. J. S. DeGRASSIE et al., *Nucl. Fusion*, **49**, 085020 (2009).

21. C. S. CHANG, S. KUE, and H. WEITZNER, *Phys. Plasmas*, **9**, 3884 (2002).

22. C. S. CHANG, S. KUE, and H. WEITZNER, *Phys. Plasmas*, **11**, 2649 (2004).

23. H. WEITZNER and C. S. CHANG, *Phys. Plasmas*, **11**, 3060 (2004).

24. C. S. CHANG, *Phys. Plasmas*, **11**, 5626 (2004).

25. S. H. HAHN, S. KU, and C. S. CHANG, *Phys. Plasmas*, **12**, 102501 (2005).

26. C. S. CHANG and S. KU, *Phys. Plasmas*, **15**, 062510 (2008).

27. W. M. STACEY, *Phys. Plasmas*, **18**, 102504 (2011).

28. W. M. STACEY, *Phys. Plasmas*, **18**, 122504 (2011).

29. M. A. MAHDAVI et al., *Phys. Plasmas*, **10**, 3984 (2003).

30. R. J. GROEBNER et al., *Nucl. Fusion*, **44**, 204 (2004).

31. P. B. SNYDER et al., *Phys. Plasmas*, **16**, 056118 (2009).

32. J. LUXON, *Nucl. Fusion*, **42**, 614 (2002).

33. W. M. STACEY, *Contrib. Plasma Phys.*, **48**, 94 (2008).

34. W. M. STACEY, *Fusion Plasma Physics*, pp. 85–89, Wiley-VCH, Weinheim, Germany (2005).

35. W. M. STACEY, *Phys. Plasmas*, **15**, 052503 (2008).

36. T. N. CARLSTROM, G. L. CAMPBELL, and J. C. DeBOO, *Rev. Sci. Instrum.*, **63**, 4901 (1992).

37. P. GOHIL, K. H. BURRELL, and R. J. GROEBNER, *Proc. 14th Symp. Fusion Engineering*, San Diego, California, 1991, Vol. 2, p. 1199, Institute of Electrical and Electronics Engineers (1992).

38. W. M. STACEY and R. J. GROEBNER, *Phys. Plasmas*, **15**, 012503 (2008).

39. B. A. GRIERSON et al., *Rev. Sci. Instrum.*, **81**, 10D375 (2010).

40. B. A. GRIERSON et al., *Phys. Plasmas*, **19**, 056107 (2012).

41. J. A. BOEDO et al., *Phys. Plasmas*, **18**, 032510 (2012).

42. S. H. MUELLER et al., *Phys. Plasmas*, **18**, 072504 (2011).

43. W. M. STACEY, *Phys. Plasmas*, **15**, 012501 (2008).

44. W. M. STACEY and R. J. GROEBNER, *Nucl. Fusion*, **51**, 063024 (2011).